Journal of the European Ceramic Society 42 (2022) 5893–5903

Contents lists available at ScienceDirect

Journal of the European Ceramic Society

journal homepage: www.elsevier.com/locate/jeurceramsoc

Damage tolerance in additively manufactured ceramic architected materials

Raphael Thiraux [a], Alexander D. Dupuy [a], Tianjiao Lei [a], Timothy J. Rupert [a,c], Ali Mohraz [a,b], Lorenzo Valdevit [a,c,*]

[a] Materials Science and Engineering, University of California, Irvine, CA 92697, USA
[b] Chemical and Biomolecular Engineering, University of California, Irvine, CA 92697, USA
[c] Mechanical and Aerospace Engineering, University of California, Irvine, CA 92697, USA

ARTICLE INFO

Keywords:
Direct ink writing
Additive manufacturing
Alumina
Architected materials
Damage tolerance

ABSTRACT

Technical ceramics exhibit exceptional high-temperature properties, but unfortunately their extreme crack sensitivity and high melting point make it challenging to manufacture geometrically complex structures with sufficient strength and toughness. Emerging additive manufacturing technologies enable the fabrication of large-scale complex-shape artifacts with architected internal topology; when such topology can be arranged at the microscale, the defect population can be controlled, thus improving the strength of the material. Here, ceramic micro-architected materials are fabricated using direct ink writing (DIW) of an alumina nanoparticle-loaded ink, followed by sintering. After characterizing the rheology of the ink and extracting optimal processing parameters, the microstructure of the sintered structures is investigated to assess composition, density, grain size and defect population. Mechanical experiments reveal that woodpile architected materials with relative densities of 0.38–0.73 exhibit higher strength and damage tolerance than fully dense ceramics printed under identical conditions, an intriguing feature that can be attributed to topological toughening.

1. Introduction

The need for high performance materials with increased temperature resistance, improved mechanical strength and reduced density is a major driving force for materials research, motivated by applications in a wide range of industries, from transportation to aerospace and defense systems. For example, even a modest increase in the high-temperature performance of materials in propulsion systems would significantly raise the fuel efficiency of the engine, with great economical and environmental impact. By virtue of their strong covalent and ionic bonds, technical ceramics exhibit outstanding mechanical properties at high temperature [1,2], and would be exceptional candidates for these applications. Unfortunately, though, their extreme crack sensitivity, coupled with the inevitable introduction of flaws during processing, strongly limits the achievable strength, currently hindering most structural applications in mission critical components. Over the past 50 years, several approaches have been successfully demonstrated to reduce the flaw sensitivity of ceramics and increase their fracture toughness, including transformation toughening and the design of ceramic matrix composites, where toughness is increased via crack deflection, crack bridging and fiber pullout [3]. Yet, in most material systems, the strength of ceramics is still much lower than the theoretical value, often by more than one order of magnitude.

One approach to achieve theoretical strength in ceramics is to reduce the size of the sample to such a small scale that the internal cracks are too small to grow. This approach has been recently demonstrated for silicon oxycarbide (SiOC) and carbon, produced by two-photon polymerization Direct Laser Writing (2pp-DLW) of a suitable pre-ceramic resin followed by pyrolysis [4–6], with ceramics exhibiting compressive strengths in excess of 7 GPa. The main shortcoming of this approach is that samples need to be smaller than a critical length scale, typically in the 100 nm – 10 μm range. One avenue towards scale-up is to design and fabricate micro/nano-architected materials, i.e., periodic repetitions of generally identical unit cells along three directions, where the unit cell architecture is optimized for mechanical efficiency and the feature size within the unit cell is sufficiently small for the material to locally achieve theoretical strength. This approach has also been recently demonstrated and has allowed fabrication of porous architected materials with

* Corresponding author at: Materials Science and Engineering, University of California, Irvine, CA 92697, USA.
E-mail address: Valdevit@uci.edu (L. Valdevit).

https://doi.org/10.1016/j.jeurceramsoc.2022.05.059
Received 28 December 2021; Received in revised form 12 May 2022; Accepted 23 May 2022
Available online 27 May 2022

unprecedented combinations of high strength and low density [6–12] and sample sizes as large as 30 μm [13].

While 2pp-DLW has allowed demonstration of exceptional combinations of properties in ceramic architected materials, the maximum achievable sample size is still far too small for any realistic structural application. Significant scale-up can be enabled by using Direct Ink Writing (DIW), an additive manufacturing (AM) approach whereby an ink is extruded at room temperature through a nozzle and deposited in the form of lines that can be architected in three dimensions. DIW has been successfully used to deposit a wide range of material systems, from metals [14] to biopolymers [15] and composites [16–18]. Most inks consist of a suspension of colloidal particles stabilized by the aid of a dispersant, with a rheological modifier to provide the ink with high yield stress and shear thinning behavior, two characteristics that are crucial for achieving excellent quality prints. If ceramic particles are introduced in the ink, and the structure is sintered after printing, high-quality ceramic architected materials can be produced. DIW is a relatively fast approach with high dimensional accuracy, allowing fabrication of structures with overall dimensions at the cm scale and feature sizes (line diameter) down to ~200 μm, in 5–15 min. While these feature sizes are still too large to expect theoretical strength from the constituent ceramic, they are small enough to result in significantly better mechanical properties than at the macroscale.

While DIW is somewhat limited in achievable structural complexity relative to other AM approaches, due to the inability to interrupt the flow of material during printing and the limited span that printed lines can sustain without collapsing, recent work has resulted in several innovative solutions, from laser-assisted printing [14], to fast solvent drying [19,20] and printing embedded in a viscoelastic fluid [21], reducing the gap between DIW and other AM approaches.

In this work, an ink is developed that is optimized for printing of architected materials, and results in pure aluminum oxide (Al_2O_3) upon sintering. This ink is used to fabricate woodpile structures, simple architected materials consisting of periodic repetitions of layers of lines arranged in a 0/90° sequence. While this topology is not as structurally efficient as other lattice designs (e.g., the octet lattice [22]), it allows us to investigate the effect of topology on the failure mechanisms of ceramic architected materials. After characterizing the stiffness and theoretical strength of the constituent material via nanoindentation, the strength and failure behavior of woodpile structures with different feature sizes and relative densities are quantified. The results are correlated with microstructural features (including the presence and location of defects in the prints) and interpreted with the aid of simple mechanical models. Topological features in the architected material design are found to be effective at controlling the crack path during failure: remarkably, this enables fabrication of structures that can be much stronger than heavier solid materials printed and sintered under identical conditions, or structures that can fail graciously, displaying a level of damage tolerance that is extremely unusual for ceramics. While results are exclusively presented for alumina woodpile structures, the mechanical effects unveiled in this work are general and will apply to different architected materials topologies and constituent ceramics.

2. Experimental procedures

2.1. Raw materials and ink preparation

The ceramic ink was composed of four materials: (i) Grade A-16 SG alumina powder, with an average reported particle size of 0.5 μm (Almatis, USA), (ii) Ammonium polyacrylate (NHPA) (Darvan 821 A, R. T. Vanderbilt Company, USA), used as a dispersant, (iii) 1-ethenyl-2-pyrrolidinone (PVP) homopolymer (Sigma-Aldrich, USA), used as a rheology modifier, and (iv) DI water used as solvent. This chemistry, originally proposed by Lisa *et al.* [23], has two key advantages over alternative compositions: the pH, which controls the cohesion between the colloids, remains constant and slightly higher than the particles' isoelectronic point throughout mixing, [24,25] creating repulsion between the particles and stabilizing the suspension, thus eliminating the need for continuous pH adjustments; furthermore, all components have low toxicity, thus facilitating the manufacture of parts as no special safety equipment or chemical disposal is required.

Relative to the composition reported by Lisa *et al.* [23], the volume fractions of the ink components were adjusted to achieve a higher yield stress and storage modulus, while maintaining the desired shear-thinning behavior of the ink. A larger storage modulus allows deposition of longer suspended features [26] and a larger yield stress enables printing of taller structures [27], both of which facilitate the printing of lightweight architected materials. The final chemical composition of the ink was 53 vol% Al_2O_3, 9.9 vol% PVP, 4.2 vol% NHPA and 32.9 vol% DI water. NHPA was first mixed with DI water in a vortex mixer (Vortex-Genie, Scientific Industries, USA) for 30 s. The alumina powder was sieved with a 100-micron sieve to eliminate large agglomerates, and gradually added to the solution and mixed in a planetary centrifugal mixer (AR100, Thinky, USA) for 20 s at 2000 rpm. While the viscosity was still low, the ink was placed in a vacuum chamber to remove most bubbles. As each step of the mixing process results in some loss of water (which varies from batch to batch), the mass of the ink was measured before and after each step and water was added as needed, to maintain the target proportions. PVP was subsequently added to the solution and mixed using a planetary centrifugal mixer at 2000 rpm for 60 s. The ink was exposed to vacuum again and then carefully loaded in the syringe using a flat spatula to minimize the introduction of bubbles. Finally, the ink was transferred to a new and clean syringe using a luer-lock style connector and the syringe was placed back inside the planetary centrifugal mixer with an adapter and left to defoam for 300 s

2.2. Rheological measurements

The rheological properties of the ink were measured with an AR-G2 rheometer (TA Instruments, USA), equipped with a standard 40 mm sand-blasted parallel plate geometry with a gap of 1 mm. A solvent trap was used to reduce the evaporation of the DI water during the experiment. A flow ramp was applied with shear rates ranging from 100 to 0.1 s^{-1} (and then back to 100 s^{-1}), to capture the evolution of the shear stress and the viscosity as a function of the shear rate. The flow parameters were extracted on the ramp down of the test, in the range from 40 to 0.1 s^{-1}, as secondary flow could appear at high shear rates, altering the results. To ensure good statistics, all parameters were averaged over eight different tests. Subsequently, stress amplitude sweep measurements at a frequency of 1 Hz were conducted in the range of 1 Pa to 4000 Pa, to extract the storage and loss moduli as a function of the applied stress.

2.3. Direct Ink Writing (DIW) procedure and sintering

All structures were built using a custom ceramic DIW printer, composed of a 3-axis motion stage (Aerotech, USA) and an air-powered fluid dispensing system (Ultimus V, Nordson EFD, USA). The linear stages were stacked on top of each other, assembled and calibrated by Aerotech, resulting in a volumetric accuracy of 10 μm^3 and a 10 cm × 10 cm × 10 cm maximum build volume. The air-powered fluid dispensing system delivered a maximum pressure of 689 kPa. The syringe was stationary on the gantry system, which was assembled with optical-quality structural components (Newport Inc, USA) and mounted on an optical table to reduce vibrations. The gcode for all prints was programmed in the Aerobasics environment. The geometry and build parameters were programmed using a modified version of the code provided in the technical note by William et al. [28] Our Direct Ink Writing system has three controllable printing parameters: (i) layer thickness, (ii) dispensing pressure, and (iii) tabletop speed. The first parameter was set to 85% of the nozzle diameter, to ensure good layer-to-layer contact. The other two parameters must be carefully

controlled to achieve the best compromise of printing speed and quality [29]. To choose the optimal tabletop speed for any given dispensing pressure, the mass flow rate was measured as a function of the applied pressure, by weighing the amount of ink extruded under a constant pressure drop for 20 s. The tabletop speed was extracted by dividing the mass flow rate by the area of the nozzle and the density of the ink. Each measurement was repeated three times to ensure consistency. A new nozzle was used for each measurement to minimize errors from possible drying of the ink between measurements. The test was performed for three different nozzle diameters: 410 μm, 580 μm and 840 μm. For each nozzle diameter, a direct relationship was obtained between the pressure and the tabletop speed, enabling selection of printing parameters that allow extrusion of lines with thickness equal to the corresponding nozzle diameter. Three sets of those extrusion parameters were selected and validated with printing of actual structures. By observing the print quality, the printing time, and the success rate, an optimal set of parameters was finally assessed.

In this study, both fully dense cubes and woodpile structures were printed, using the same nozzle sizes as previously discussed. The structures were printed by layer-by-layer deposition of lines, changing printing orientation by 90 degrees at each layer. The distance between the lines, henceforth called gap (g) and equivalent to the pitch (p) minus the diameter (d), in the woodpile structures was chosen to be equal to one or two times the diameter (d_n) of the nozzle (Fig. 1). As the relative density of a woodpile structure can be approximated as $\overline{\rho} = \frac{\pi}{4}\frac{d}{p}$, samples with a pitch of two and three times the diameter have theoretical relative densities of 39% and 26%, respectively. The pitch for the fully dense specimens was chosen as 80% of the line diameter, to minimize internal porosity [30]. The dimensions of all prints were 1 cm × 1 cm × 1 cm. To demonstrate the smallest features that can be obtained with this ink, 5 mm × 5 mm × 5 mm woodpile structures were also printed with a 200 μm nozzle, although full characterization was not performed on these structures.

All printed parts were conventionally sintered in air using a muffle furnace (Lindberg, USA). A multistep sintering schedule was employed to ensure that all binders and organics were eliminated prior to sintering. First, the samples were heated up at a rate of 5 °C/min to 700 °C and held at this temperature for 1 hr to burn off the polymer. Subsequently, the specimens were heated at the same rate up to 1600 °C and held at this temperature for 1 hr to ensure complete densification. Finally, they were cooled down to room temperature at a rate of 5 °C/min. Bulk density measurements of the alumina were performed on both fully dense and woodpile structures using the Archimedes method.

2.4. Material characterization and mechanical measurements

Microstructure and grain size information was acquired from fracture surfaces of specimens using a FEI Magellan 400 XHR scanning electron microscope (SEM), operated at 3 kV. Computed tomography (CT) scans were performed using a Xaria 410 Versa (Zeiss, USA) with a voltage of 55 kV and a resolution of 15 μm.

Nanoindentation tests were performed on the bulk sintered samples using a Nano Indenter G200 (Agilent Technologies). For each sample, at least 20 indentations were performed with a maximum load of 200 mN. The distance between the two nearest indents was 30 μm, which was larger than 30 times the penetration depth (~700 nm), thus avoiding interference. The hardness (H) was extracted from the unloading section of the load-displacement curves as $H = P/A$, with P the load applied on the sample surface and A the projected contact area at that load. The Young's modulus ($E_{Al_2O_3}$) was also obtained from the unloading curve as $\frac{(1-\nu^2)}{E_{Al_2O_3}} = \frac{1}{E_r} - \frac{(1-\nu_i^2)}{E_i}$, where ν and ν_i correspond to the Poisson's ratio of the sample (assumed to be = 0.2 for alumina) and the indenter (= 0.07), respectively, and E_i is the Young's modulus of the indenter (= 1141 GPa); E_r is the reduced modulus, $E_r = \frac{\sqrt{\pi}S}{2\beta\sqrt{A}}$, where β is a constant related to the indenter geometry (= 1.034), and S is the elastic stiffness of the contact and obtained from the slope of the initial 50% of the unloading curve. To minimize the effect of structural compliance, woodpile structures were tested in the regions corresponding to columns of multiple line intersections (red regions in Fig. 1b).

Macroscopic compression tests were performed on the bulk sintered samples using an Instron 8800 servo-electric Universal Test Frame, equipped with a 100 kN load cell. A constant displacement rate of 0.033 mm/s was used for all tests. Images of the samples were collected using a camera (Point Grey, USA) from the digital image correlation system (Correlated Solutions, USA) every 300–500 ms during the test, to provide information on the deformation sequence and the failure mechanisms. Those images are synchronized with the load and displacement measurements from the Instron machine. The nominal sample dimensions are used to calculate the stress and strain. A polymeric pad was interposed between the sample and the top compression plate (the bottom being already flat since the specimen was printed directly on a flat surface), to minimize the risk of premature failure due to stress intensifications related to sample non-planarity.

3. Results and discussion

3.1. Rheological properties of the ink

The rheology of the ink is crucial to ensure its printability. For DIW, suitable inks must possess two essential features: (i) a suitable yield stress and (ii) a shear thinning behavior. Fluids that possess these features can generally be described by the Herschel-Bulkley model [31]:

$$\sigma = \sigma_0 + K\dot{\gamma}^n \quad (1)$$

where σ and σ_0 are the applied shear stress and the yield stress in shear (Pa), respectively, $\dot{\gamma}$ is the applied shear rate (s^{-1}), K is the consistency index ($Pa.s^{-1}$) and n is the flow behavior index (dimensionless). The ink is shear thinning for $n < 1$, Newtonian for $n = 1$ and shear thickening for $n > 1$. A shear thinning behavior indicates a decrease of viscosity with increasing shear rate, thus facilitating the flow through and out of the nozzle. At the same time, the yield stress must be sufficiently large for the ink to not flow under its own weight when inside the syringe and to maintain its shape after deposition. During extrusion, the shear stress

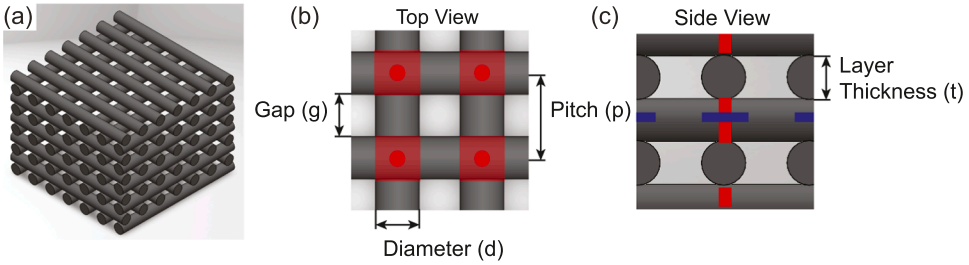

Fig. 1. Computer-Aided Design CAD model of the woodpile structure, presented as (a) perspective, (b) top and (c) side view. The red shaded regions represent the area in contact between layers. The red and blue dashed lines represent the columns and bridges, respectively.

increases along the radius of the nozzle. Consequently, the flow profile is typically composed of a solid core experiencing stress lower than the yield stress, and an outer layer experiencing shear-thinning behavior.

The parameters of the Herschel-Bulkley equation are extracted from a flow curve, where the shear rate is progressively decreased while the shear stress is measured. The results are reported in Fig. 2a. The behavior of the ink is clearly shear thinning, characterized by an average yield stress, $\sigma_0 = 602$ Pa and an average flow behavior index, $n = 0.7$.

The yield stress of the viscoelastic ink can also be independently estimated by an analysis of the evolution of storage and loss moduli (G' and G", respectively) of the material as a function of an applied oscillatory stress (Fig. 2b). For $\sigma < 1$ kPa, the ink displays a plateau in G' with a value that is about an order of magnitude larger than G", indicating solid-like viscoelastic behavior. At larger stresses, the gap between G' and G" narrows, indicating a decrease in the fraction of recoverable strain and a gradual transition toward a viscoelastic liquid. Finally, at $\sigma \sim 1$ kPa, both moduli precipitously drop, and the trend is inverted (G' < G"), indicating a transition to liquid-like behavior. Hence the transition point, $\sigma \sim 1$ kPa, can be taken as a measure of the yield stress of the ink. Importantly, the value of the zero-shear storage modulus ($G'_0 \sim 300$ kPa) is sufficiently large to avoid line deflection while printing the woodpile structures. We emphasize that a careful rebalancing of the volume fractions of polymer, water, and alumina relative to the amounts used in Lisa et al. [23] resulted in an ink with a yield stress ~5 times larger, suggesting that the formulation presented herein is much more suitable for fabrication of architected materials.

3.2. Extraction of optimal printing parameters

The optimal relation between applied pressure and tabletop speed is extracted for three nozzle sizes (410 μm, 580 μm and 840 μm), as detailed in Section 2.3, and plotted in Fig. 3a. While the nozzle size does not have a significant impact on the pressure-speed relation, these small disparities may influence the quality of the print. Notice that at high pressure the tabletop speed tends to asymptote, indicating a progressive difficulty in extruding the ink at higher speeds. This phenomenon can be tentatively attributed to jamming of the particles near the nozzle tip resulting in a filtering effect, and/or local shear thickening of the concentrated suspension.

While all combinations of pressure and tabletop speed depicted in Fig. 3a are in principle capable of generating successful prints, not all conditions are equally effective. Increasing the pressure considerably reduces the print time, but excessive pressures will result in extrusion difficulty, as noted above, with potentially deleterious effects on printing performance and/or part quality. The implication is that an optimal printing pressure must be identified. To estimate this value, three sets of pressures / tabletop speeds were selected and used to print test samples at different nozzle sizes. All test samples are woodpile structures with gap equal to the line diameter, allowing accurate evaluation of the geometric fidelity of the process. The samples printed with a pressure of 69 kPa did not result in successful samples (Fig. S1). We observe that pressures of 138 kPa and 207 kPa can generate high quality prints (Fig. 3b). However, at higher pressure (207 kPa), the nozzle clogs more often than at lower pressures, resulting in a lower success rate for the prints. Additionally, high pressure results in over-deposition at the end of the woodpile where the nozzle turns around, resulting in the

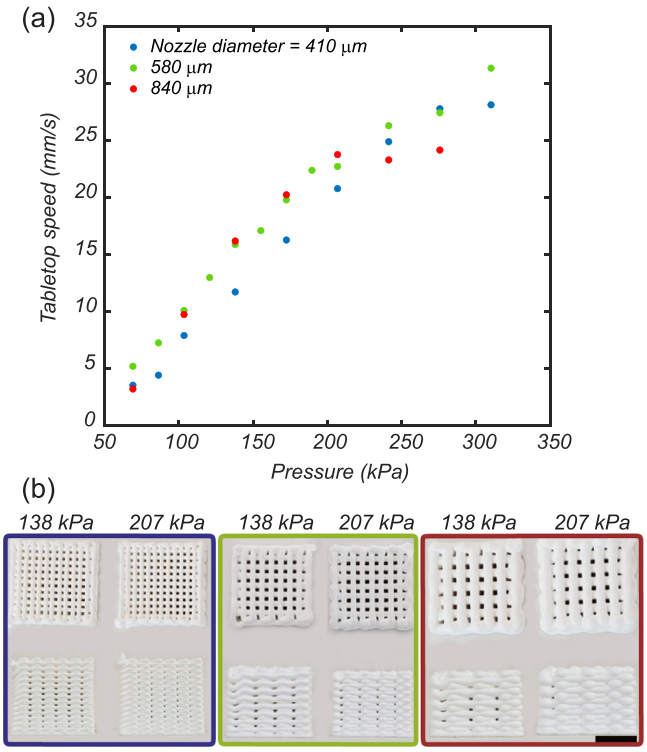

Fig. 3. (a) Relationship between the tabletop speed and the pressure applied for different nozzle diameters (410 μm, 580 μm and 840 μm). (b) Green bodies of woodpile structures printed for different pressures and nozzle sizes. Scale bar: 5 mm.

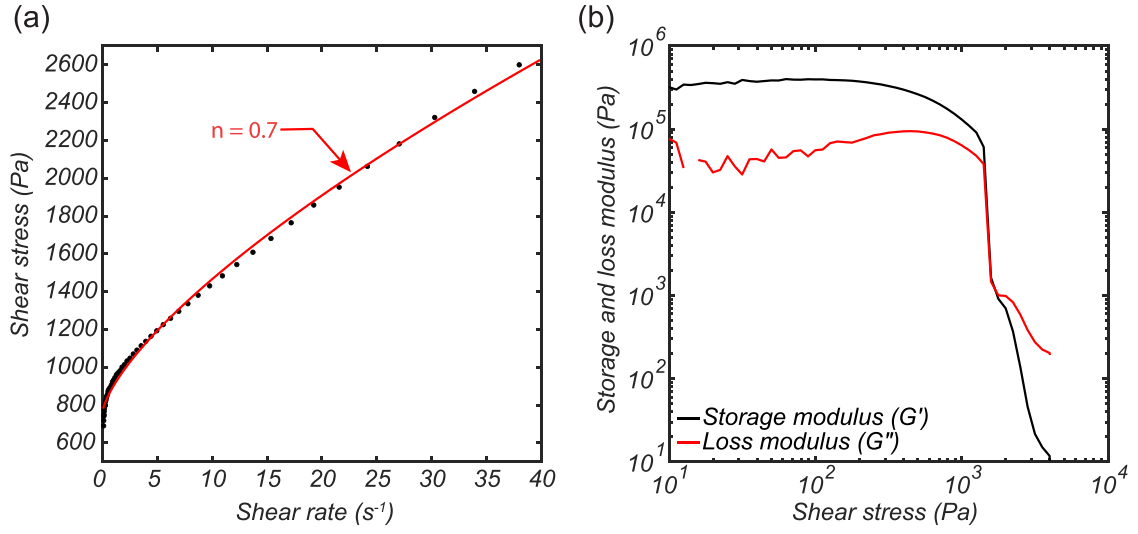

Fig. 2. (a) Shear stress vs shear rate for the alumina ink. (b) Storage and loss moduli for the alumina ink, showing a yield stress of ~10^3 Pa.

formation of a nearly dense outer layer: this compromises geometric accuracy, wastes ink and may result in undesired crack nucleation sites. Among the three pressures tested, a pressure of 138 kPa is the most suitable to achieve good and repeatable quality prints, while minimizing the printing time.

Fig. 4a shows a slice from a cross sectional CT scan of the woodpile structure printed with a 580 μm nozzle and a gap nominally equal to the line diameter. Only the lines printed perpendicular to the image plane are shown in the scans. The lines are numbered from the lowest to the highest in the direction of printing, represented with the black arrow. Notice that the lines have a larger diameter (~650 μm) and smaller gap (~300 μm) for the first two layers, as shown in Fig. 4b. Subsequently, the dimensions stabilize to a diameter of ~500 ± 34 μm and a gap of ~400 ± 54 μm, demonstrating good print quality. The steady-state values of both line diameter and gap are lower than the design values, a discrepancy that can be attributed to the drying and sintering of the structure. The large line diameter at the beginning of the print (~650 μm) can be attributed to two reasons: (i) the flow needs some time to stabilize after initiation and (ii) the layer in contact with the substrate (layer 0, not shown on the scan) is intentionally more compressed to ensure good adhesion. Fig. 4c shows a plot of greyscale values along the path denoted by the red arrow in Fig. 4a. For more clarity, the scan has been converted to a binary image before extracting the histogram (with 1 representing the line and 0 the gap in between). This demonstrates that consistent periodicity was also achieved in the vertical direction.

To better understand the impact of nozzle geometry and ink properties on the optimal printing parameters, the relationship between applied pressure and tabletop speed is analytically modeled. For a given pressure, the shear rate increases with decreasing nozzle diameter. While in a cylindrical nozzle the shear rate is uniform along the nozzle length, in a conical nozzle (as the ones adopted in this study) the maximum value of the shear rate is reached only at the exit, making it more suitable for the extrusion of high viscosity materials. The flow rate of a viscoelastic material following the Hershey-Bulkley behavior in a conical nozzle can be approximated as follows [32]:

$$Q = \frac{\pi d_i^3 d_o^3}{256}\left[\frac{3n \quad tan(\theta) \quad \left(\Delta P - \frac{2\sigma_0}{tan \quad (\theta)} ln \quad \frac{d_i}{d_o}\right)}{2K\left(\frac{d_i^{3n} - d_o^{3n}}{2^{3n}}\right)}\right]^{1/n} \tag{2}$$

where ΔP is the pressure drop along the nozzle length, d_i and d_o are the diameters at the entrance and exit of the nozzle, respectively, θ is the angle of the nozzle, and K, n, and σ_0 are the rheological parameters of the ink. Finally, the flow rate can be trivially related to the tabletop speed (V) as $V = 16Q/\pi t^2$, where t is the line thickness. It is assumed that under optimal printing conditions, the diameter of the line (d) equals the nozzle diameter (d_n).

In Fig. 5a, the experimentally derived pressure-tabletop speed relations (from Fig. 3a) are compared to the model (black line), using the Herschel-Bulkley parameters extracted from the rheological measurements. As expected, our experimental data are in good agreement with the model at low pressure. As the pressure is increased, the experimental data starts plateauing and diverges from the model. This discrepancy could be attributed to multiple causes, including the use of a parallel plate geometry for the rheological measurements (resulting in variable shear rate along the radius), the fact that the model does not account for the actual surface roughness of the syringe and conical nozzle, the possibility that particles experience jamming and self-filtration in the converging flow, or shear thickening at the exceedingly high shear rates near the nozzle tip (see below). Despite these disagreements at higher pressure, this data demonstrates the usefulness of first-order analytical models in extracting optimal printing parameters from simple rheological experiments. The maximum shear rate experienced by the ink at any section of the nozzle was calculated along the nozzle length for different values of the dispensing pressure (Fig. 5b). Notice that the shear rate significantly increases closer to the tip and this increase happens further upstream in the nozzle at higher pressure. The dark red area in Fig. 5b indicates the region of the nozzle where the shear rate is higher than 40 s^{-1}. In this regime, the behavior of the ink becomes harder to experimentally characterize, as the centrifugal forces in the rheometer start expelling ink from the plates. This region is present for every nozzle size and for every pressure studied here. The important implication on the selection of optimal printing parameters is that a trade-off must be sought between the evaporation of the solvent resulting in clogging of the nozzle at low pressure, and the dominance of high shear rate in the nozzle causing a resistance to flow at high pressure. We observed that good printing quality is obtained at the pressure ranges in which experiment, and model are in good agreement. At higher pressures, a significant amount of ink experiences high shear rates at the nozzle tip, triggering the secondary effects described above, and resulting in lower print quality.

This understanding of the ink rheology and its behavior inside the conical nozzle allows the printing of highly dense ceramic woodpile structures with small feature sizes. Fig. 6 shows two examples of alumina woodpile structures printed with a 200 μm diameter nozzle, differing in the gap size (equal to one or two times the nozzle diameter) and hence in relative density. Notice that the gap in the printed and sintered structures (103 ± 10 μm and 254 ± 22 μm for the single-diameter and double-diameter structures, respectively) is smaller than the programmed value, consistent with findings reported in Fig. 4. Nonetheless, we note that even at this small nozzle diameter, which approaches the printability limit for such a highly loaded ink, the diameter of the line (236 ± 6 μm and 259 ± 22 μm for the single and double gap structures, respectively) is close to the size of the nozzle diameter.

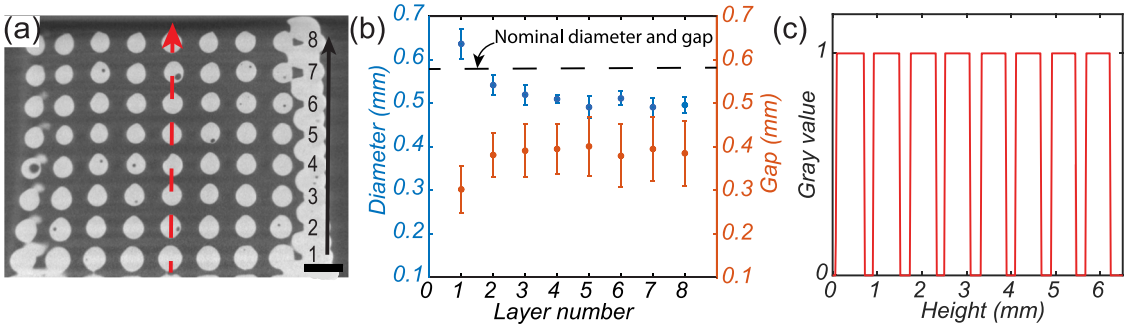

Fig. 4. (a) CT scan of the cross section of the alumina woodpile structure printed with a 580 μm nozzle and a gap nominally equal to the line diameter. The black arrow represents the build height direction. (b) Evolution of the diameter and the gap with the printed layer (dimensions are averaged over all lines in a layer). (c) Plot of greyscale values along the red dashed line, indicating excellent periodicity. Scale bar: 1 mm.

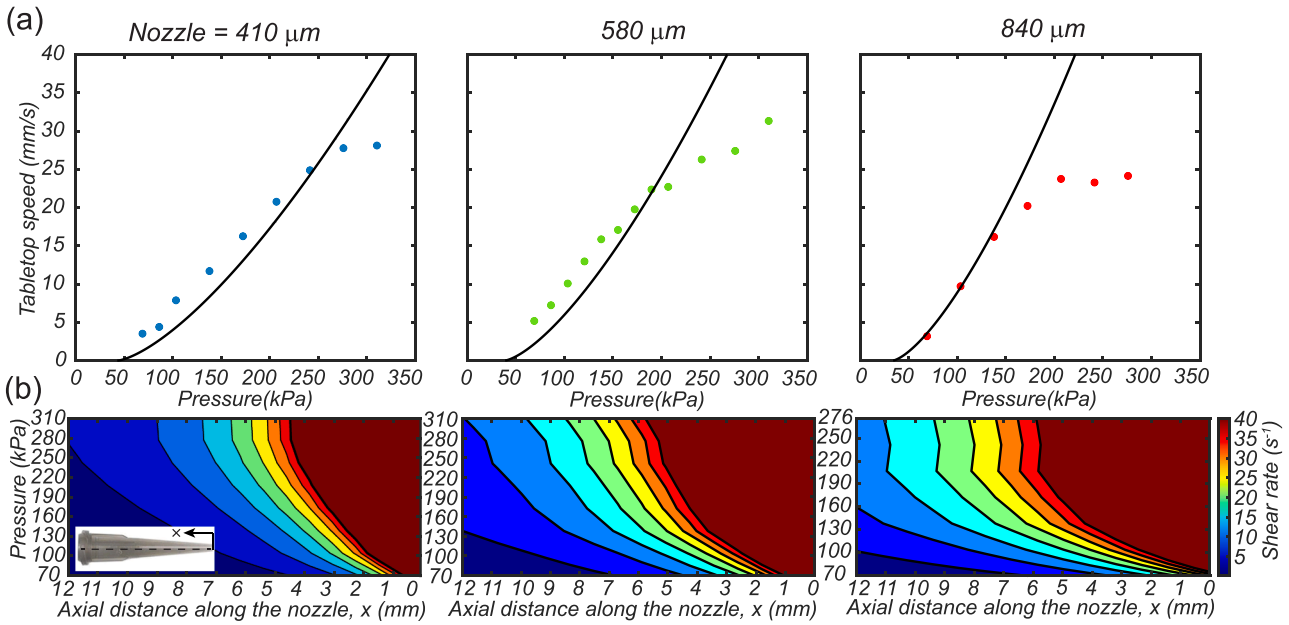

Fig. 5. (a) Comparison between the analytical model and the experimental measurements. (b) Map of the maximum shear rate along the conical nozzle, at different dispensing pressure values. Results are presented for three nozzle diameters: 410 μm, 580 μm and 840 μm.

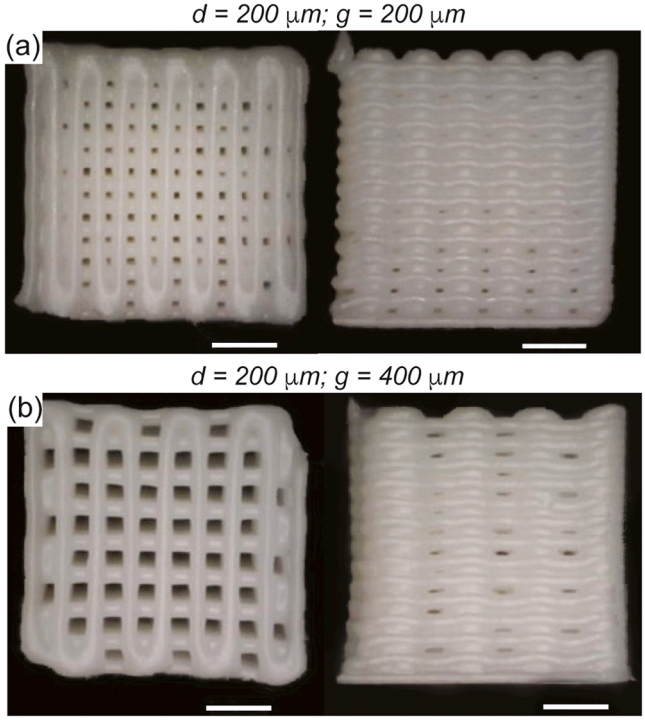

Fig. 6. Woodpile structures manufactured using the 200 μm nozzle with (a) a pitch equal to the line diameter and (b) a pitch that is twice the line diameter. Scale bar: 1 mm.

3.3. Microstructural evolution

Fig. 7 shows fracture surface SEM micrographs of a woodpile structure (Fig. 7a) and fully dense specimen (Fig. 7b) after sintering, both printed with a 580 μm nozzle. A large pore on the inner surface of the woodpile structure is shown in Fig. 7c. The bulk density and average grain size for the strut of the woodpile structure and the fully dense specimen are similar. The bulk density is found to be around 98% of the theoretical density of alumina. This excellent bulk density value (low porosity) is attributed to the fine particle size distribution of the powder and the high temperatures used during sintering. From the micrographs, we extracted an average grain size of 2.22 ± 1.25 μm for the woodpile structures printed with the 580 μm nozzle size, 2.80 ± 1.39 μm for those printed with the 410 μm nozzle (not shown on the figure) and 1. 9 ± 0.9 μm for the fully dense specimen. The grain size inside the large pore is the same as the grain size calculated on the fracture surfaces, indicating that the distribution of the grain size is homogeneous throughout the sample. Two different types of pores are observed, corresponding to defects at two different length scales. The largest pores range from several hundred microns to ten microns and are often randomly distributed. The surface of a representative large pore is depicted in Fig. 7c. These pores originate from the ink preparation and the formation of bubbles. Pores smaller than 1 μm are observed between grains (Fig. 7a) and are attributed to residual porosity left over after sintering.

Computed tomography (CT) scans are extracted to investigate the quality of the print. Fig. 8 shows representative slices of the CT scan for fully dense samples (Fig. 8a-b) and woodpile structures (Fig. 8c), after sintering. All scans were taken parallel to the platform, with the line direction for the fully dense specimens indicated by an arrow. Flaws and defects are visible as darker regions in the CT scans. A few important observations can be extracted:

(a) Whereas in ideal woodpile structures each pair of adjacent layers is connected by individual points (see Fig. 1), the choice of a layer thickness lower than the line diameter and the relaxation that follows ink deposition leads to extensive overlap between layers. As a result, two adjacent layers are observable in a single CT slice, with both horizontal and vertical lines (Fig. 8c).
(b) Both the fully dense and woodpile samples show uniform shades of gray throughout the sample, indicating homogeneous sintering.
(c) Different types of defects can be clearly identified. (i) *Delaminations*, which can be observed as dark shadows moving through the slice (Fig. 8a and Movie 1 in Supplementary Information), are only observed in the fully dense sample and form during sintering. (ii) *Cracks* are only present in the fully dense samples (Fig. 8b) and do not follow the printing direction. (iii) *Pores* are present and randomly distributed in both structures. In

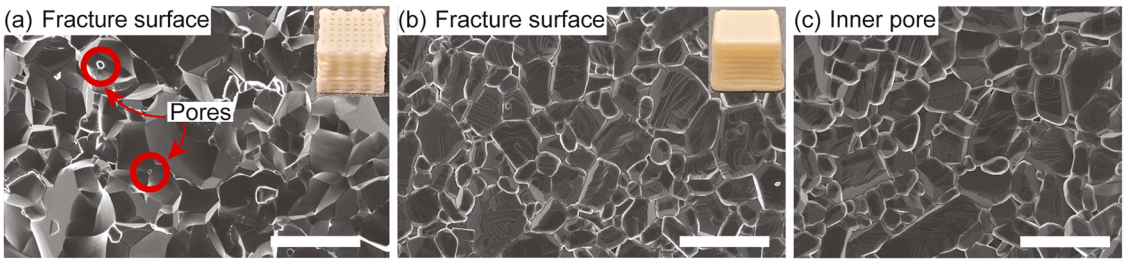

Fig. 7. Scanning electron micrographs of sintered alumina structures printed with a 580 μm nozzle size: (a) fracture surface of a woodpile structure; (b) fracture surface of a fully dense sample; (c) inner surface of a large pore in the woodpile structure. Notice that the grain size is ~2 μm in all specimens. Scale bar: 5 μm.

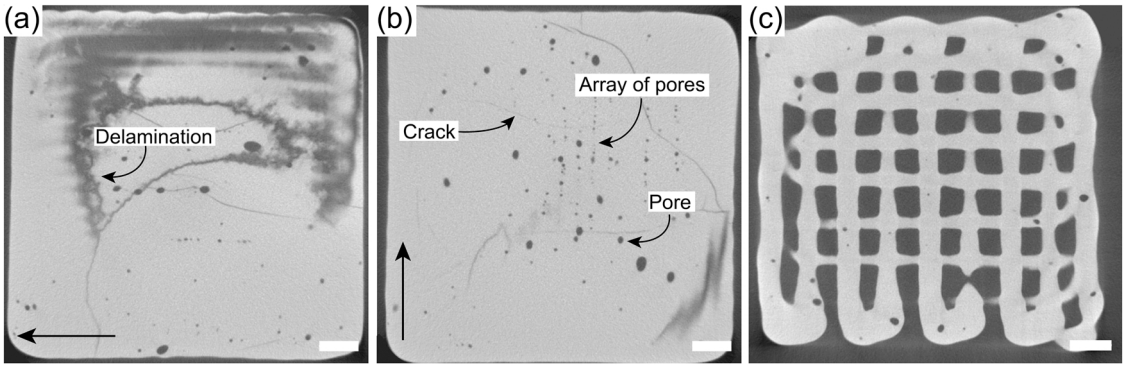

Fig. 8. CT scans of sintered alumina structures: fully dense sample showing extensive delamination (a) and rows of aligned pores (b), and woodpile structure showing isolated pores and well-sintered square connection areas between layers (c). Scale bar: 1 mm.

the woodpile structure, pores are clearly visible within the lines. Additionally, in the fully dense specimens, entire rows of pores changing direction by $+/-90^{\circ}$ from one layer to another (Fig. 8b) can also be observed. These pores are related to imperfect bonding between adjacent lines.

Supplementary material related to this article can be found online at doi:doi:10.1016/j.jeurceramsoc.2022.05.059.

While arrays of pores between adjacent lines have previously been observed in SEM micrographs of dense ceramic specimens fabricated via Direct Ink Writing [33,34], extensive delaminations between layers and curved cracks are not generally reported in the literature. While process parameter optimization may certainly mitigate the presence of these defects (e.g., increasing line overlap can eliminate inter-line array of pores [34]), we point out that these delaminations and curved cracks can only clearly be observed by CT scanning, a technique that is not routinely employed for characterization of ceramics. In any case, the lack of delaminations and curved cracks extending through multiple print lines in our woodpile structures confirm that architected material design strategies can be used to effectively control defect population, size and shape in 3D printed ceramic materials.

3.4. Mechanical properties

To explore potential size effects on mechanical properties related to the line diameter, nanoindentation is performed on a fully dense sample printed with a 580 μm nozzle diameter and woodpile structures printed with 200 μm and 580 μm nozzle diameters, respectively. The results are shown in Table 1.

The Young's moduli of the fully dense structure printed with the 580 μm nozzle, the woodpile structures printed with the 200 μm and the 580 μm nozzle are nearly identical, and in good agreement with literature values for both conventionally sintered dense alumina (340–400 GPa for sample with porosity between 0% and 2%) [35,36] and alumina samples printed via DIW (300–370 GPa for samples with porosity between 1% and 5%) [33,34]. All three samples also have nearly identical hardness (H~23 GPa), in good agreement with literature data (20–26 GPa) [37]. From Tabor's relationship [38], the theoretical strength of alumina ($\sigma^{f.th}_{Al_2O_3}$) can be estimated as $\sigma^{f.th}_{Al_2O_3} \sim H/3 = 7.5$ GPa. While this relationship is commonly applied to non-strain-hardening metals, it has also been shown to be reasonably accurate for ceramics (including Al_2O_3) under low strain rates [39,40]. Collectively, these results show that (i) sintered lines printed with different nozzle sizes have virtually the same mechanical properties (no size effect in this feature size range), and (ii) all samples are fully sintered, and reach the mechanical properties of dense alumina with minimal porosity.

Table 1
Summary of nanoindentation results on fully dense specimens and woodpile structures printed with 200 μm and 580 μm nozzles.

	Young's Modulus (GPa)	Hardness (GPa)
Fully dense sample (580 μm nozzle)	383 ± 13	22.5 ± 1.7
Woodpile structure (200 μm nozzle)	384 ± 13	23.3 ± 1.4
Woodpile structure (580 μm nozzle)	352 ± 16	22.4 ± 1.2

Several sintered woodpile structures printed with different nozzle sizes and pitches were subjected to quasi-static macroscale compression experiments, alongside a few sintered dense specimens. The actual geometric dimensions of each sample are reported in Table S1 in the Supplementary Material. Representative stress-strain curves are shown in Fig. 9, with strength and damage tolerance data presented in Fig. 10. The compression strength is extracted from the stress-strain curves at the highest stress drop that corresponds to catastrophic failure of the structure, represented as the black dots in Fig. 10. Movies with synchronous montage of the stress/strain curve with images of sample deformation and failure are available in the Supplementary Material.

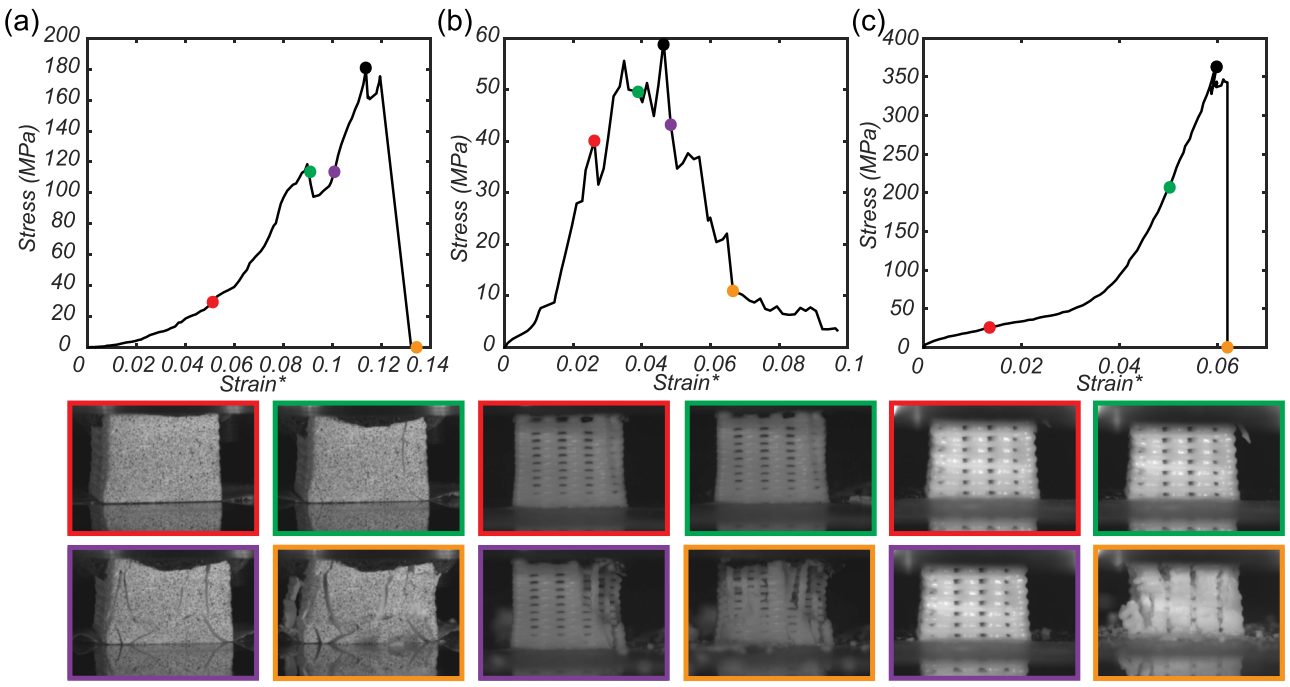

Fig. 9. Stress/strain curves of representative (a) fully dense specimen, printed with a 580 μm nozzle size and (b, c) woodpile structures, with the following characteristics: d = (410 μm, 580 μm); g = (410 μm, 580 μm); $\bar{\rho}$= (0.55, 0.59). Notice that woodpile structures can be designed to fail less catastrophically than fully dense structures (b) or to be much stronger than fully dense specimens that are twice as dense (c). The black dots represent the events used to measure the compressive strength. *Note that the strain does not represent the true strain of the specimen but rather a combination of the strain of the specimen and the elastomeric pad interposed between sample and loading plate to mitigate stress intensifications.

The relative densities experimentally measured and reported in Fig. 10a deviate quite significantly from the theoretical predictions (Tables S1 and S2 in the Supplementary Material). As previously discussed, the gap and the line diameter are smaller than the predicted ones due to drying, sintering, choice of layer thickness smaller than the line diameter to ensure good contact and relaxation of the ink after deposition, resulting in denser woodpile structures.

Supplementary material related to this article can be found online at doi:doi:10.1016/j.jeurceramsoc.2022.05.059.

Three important observations can be extracted from representative stress-strain data (Fig. 9): (1) Fully dense specimens (Fig. 9a) fail catastrophically by through-sample propagation of critical cracks, at stresses that are ~50 times lower than the theoretical strength of the material. This brittle behavior is attributed to the presence of rows of pores along the inter-line boundaries, cracks and delaminations throughout the sample (Fig. 8a, b). (2) Low-relative density woodpile structures (Fig. 9b) can be weaker than fully dense specimens, but they display damage tolerance, with gradual failure characterized by multiple sequential load drops. Each load drop corresponds to the failure of a column of material, with columns separating from the rest of the sample upon failing. This unusual behavior is attributed to the topology, whereby the separation of load-bearing elements in the sample introduces damage tolerance. (3) High-relative density woodpile structures can be more than twice as strong as fully dense specimens with only half the density. This interesting behavior is attributed to the presence of less pre-existing delamination in woodpile structures, and the absence of rows of pores and cracks that extend beyond a single line diameter. These strong woodpile structures tend to fail catastrophically, whereby a column of material fails and induces collapse of the entire structure.

From observations (2) and (3), we conclude that the mechanical behavior of our woodpile structures can be engineered by tuning their relative density: in particular, as relative density increases, our metamaterials transition from a gradual to a catastrophic failure mechanism, with corresponding tradeoffs in the mechanical properties. While graduate failure in ceramic cellular materials loaded in compression has been observed for decades in a variety of material systems, [41] to the best of our knowledge the transition in failure mode reported herein (and the ability to control it via additive manufacturing) has not been previously reported. While Martin et al. [42] observed a similar gradual failure during the compression of hydroxyapatite woodpile structures, they did not observe a transition from gradual to catastrophic failure with increasing relative density, likely due to the low strength of hydroxyapatite, leading to the premature failure of individual columns and bridges.

Simple mechanical modeling can help elucidate the impact of material properties and topological features of the architected materials on their strength and damage tolerance. When loaded along the vertical direction, only the material adjacent to the nodes, red shaded regions in Fig. 1b, contributes to the load carrying capacity of the structure. Approximating those load bearing regions as square columns of cross section $d \times d$ and length l equal to the thickness of the sample, the compressive strength of the woodpile structure can then be expressed as $\sigma_{wp} = \sigma_{col}\bar{\rho}_a$, with $\bar{\rho}_a = (d/p)^2$ the areal density of columns in the sample and σ_{col} the compressive strength of an individual column. When loaded under compression, columns can fail by brittle fracture or elastic buckling. In the former case, $\sigma_{col} = \sigma^f_{Al_2O_3}$, with $\sigma^f_{Al_2O_3}$ the brittle strength of alumina. In the latter case, the strength of a column supported by horizontal braces (the bars in the *(x,y)* plane as shown as the blue dash line in Fig. 1c) can be estimated with the theory of buckling of columns on elastic foundations [43], leading to $\sigma_{col} = \frac{\pi^2}{12} E_{Al_2O_3} (\frac{d}{l})^2 / (\frac{L_{eff}}{l})^2$, with $E_{Al_2O_3}$ the elastic modulus of alumina, l the thickness of the sample (length of the column), and L_{eff} an effective length of the column that depends on the stiffness of the elastic foundation. $\frac{L_{eff}}{l} = f(\Pi)$, where $\Pi = \frac{3\pi}{4} \frac{d}{l-d} \left(\frac{l}{d}\right)^4$. The function f is a decreasing function of Π, with $f(0) = 1$ (corresponding to the case of no horizontal braces), and $f(\infty) = 0$[43]. For the samples investigated in this study, Π ranged between 48,858 and

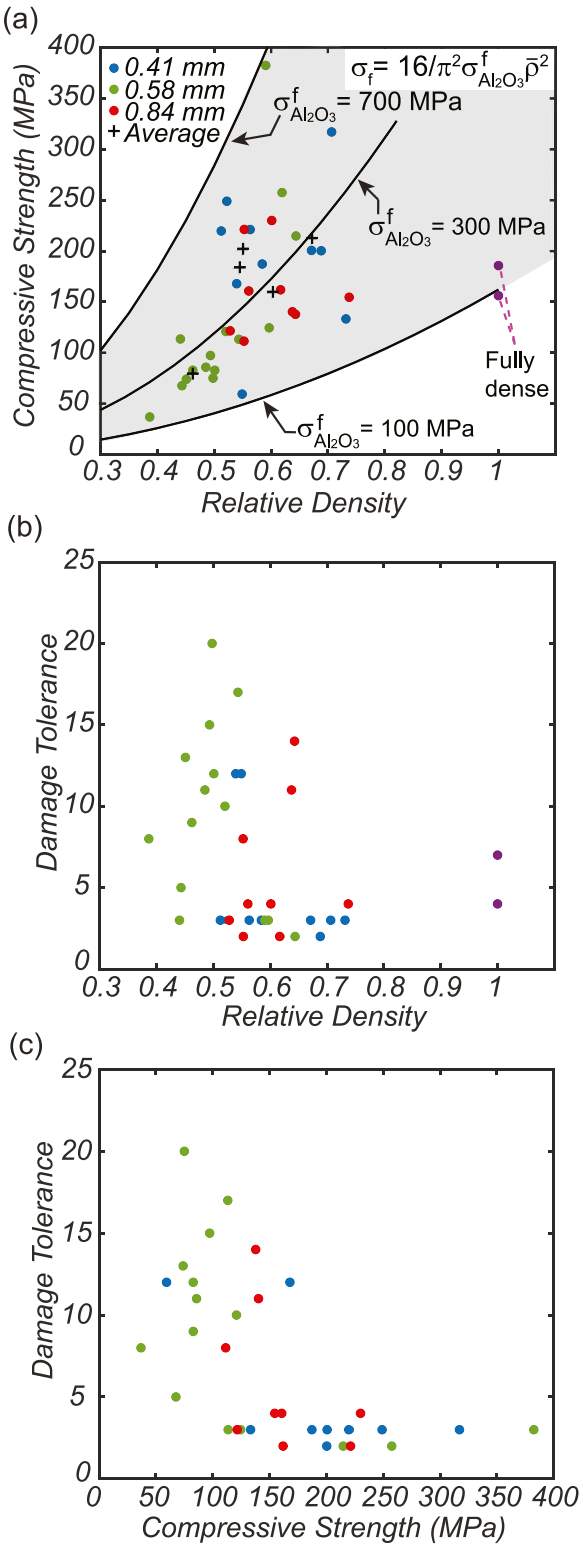

Fig. 10. (a) Compressive strength of woodpile structures and dense specimens as a function of relative density. While the scatter is significant (as expected for ceramic architected materials), the experimental data agree with a quadratic scaling, as predicted by the model (for the exact fit on experimental data, see Fig. S2). Experimental data are consistent with a fracture strength for individual alumina lines of 100–700 MPa. (b) Damage tolerance of woodpile structures (defined as the number of stress drops that lead to catastrophic failure) as a function of relative density. (c) Compressive strength cross-plotted against damage tolerance, indicating an inverse relationship between the two properties (for the exact fit on experimental data, see Fig. S2).

1448,249, resulting in $\frac{L_{eff}}{l} = 0.032 - 0.074$, and predicting buckling strength for the column in the range 4.1×10^5 - 4.0×10^4 GPa. While the value of $\sigma^f_{Al_2O_3}$ depends on the concentration of defects (pores, cracks) within the columns and is not known a priori, $\sigma^f_{Al_2O_3} < \sigma^{f,th}_{Al_2O_3} \sim 7.5$ GPa. The conclusion is that elastic buckling is never an active failure mechanism for the materials under consideration, and brittle fracture of the columns dominates. The analytical strength prediction can be plotted against the relative density of the woodpile structure for different values of $\sigma^f_{Al_2O_3}$ (Fig. 10a) and compared with measurements performed over 34 woodpile structures with different topological parameters. A value of $\sigma^f_{Al_2O_3} = 300$ MPa agrees best with the experimental results. Fitting of the experimental strength data on a power law equation yields a scaling of $\sigma_{wp} \sim \bar{\rho}^{2.2}$ (Fig. S2), in good agreement with the theoretical prediction of $\sigma_{wp} \sim \bar{\rho}^2$. The low R-squared value (R^2 =0.165) is not surprising for flaw-sensitive ceramic materials. While the scatter in the strength data is larger than in previously published studies on similar materials [41], this is partly attributed to the fact that we report the measured relative density of each specimen, as opposed to the value based on the ideal geometry.

To assess the impact of topological parameters on the damage tolerance of ceramic woodpile structures, we invoke the following mechanical argument. When a woodpile structure is loaded along the vertical direction, all columns are loaded in compression. Statistically, one column will contain the critical defect that will induce premature failure. Once a column fails, two possibilities exist: the failing column can induce failure of the adjacent columns, with resulting catastrophic failure of the entire specimen (as seen in Fig. 9c), or the failing column can separate from the adjacent columns by breaking the connecting horizontal lines without inducing failure in other columns; in the latter case, after a small load drop, the woodpile structure can continue bearing load until the next column fails. This behavior is characterized by multiple subsequent non-critical load drops (Fig. 9b) and results in damage tolerance. Fig. 10b plots the number of load drops experienced by a specimen (here taken as a proxy for damage tolerance) as a function of relative density. While the number of load drops cannot be estimated by a simple mechanical model, the experimental results seem to indicate that damage tolerance scales with the inverse of the square of the compressive strength, as illustrated in Fig. 10b (for data fit, see Fig. S2b), albeit with very large scatter. The fact that the strength of the woodpile structure scales as $\bar{\rho}^{2.2}$ and its damage tolerance scales as $\bar{\rho}^{-1.5}$ implies that strength and damage tolerance are inversely related. This is clearly observed in Fig. 10c (for data fit, see Fig. S2c). While certainly approximated, these simple mechanical models can help in the design of ceramic woodpile architected materials for specific mechanical objectives.

4. Conclusions

A new alumina-loaded polymeric ink was developed and characterized. While the rheology of the ink is not fully understood at high shear rate, a combination of experiments and simple modeling allows extraction of a suitable range of optimal parameters, in turn enabling consistent DIW and complete sintering of alumina woodpile structures with line diameters as small as 200 μm. Individual alumina lines achieve Young's modulus and theoretical strength values consistent with fully dense alumina ($E_{Al_2O_3} \sim 380$ GPa and $\sigma^{th}_{Al_2O_3} \sim 7.5$ GPa), independent of line thickness. Quasi-static compressive experiments on fully dense samples and woodpile structures with different line diameters reveal significant damage tolerance in woodpile structures, which manifests itself in two key ways: (i) high-density woodpile structures can be twice as strong and twice as light as fully dense specimens printed with identical ink and processing parameters, and (ii) low-density woodpile structures exhibit significant damage tolerance, indicated by multiple

stress drops before catastrophic failure. These intriguing features are attributed to the lack of continuous crack paths across the entire sample and the physical separation of load-bearing elements in the woodpile architecture. A simple analytical model captures the strength data and provides guidelines for optimal design. It is demonstrated that architected material topology can be used as an effective tool to control the population and the evolution of defects in additively manufactured ceramic materials, allowing tailoring of the failure mechanisms and tuning of strength and damage tolerance.

Summary of Novel Conclusions

(i) A new alumina-loaded polymeric ink is developed and characterized. A combination of experiments and simple modeling allows extraction of a suitable range of optimal parameters, in turn enabling consistent DIW and complete sintering of alumina woodpile structures with line diameters as small as 200 μm. Individual alumina lines achieve Young's modulus and theoretical strength values consistent with fully dense alumina ($E_{Al_2O_3} \sim 380$ GPa and $\sigma^{th}_{Al_2O_3} \sim 7.5$ GPa), independent of line thickness.

(ii) Quasi-static compressive experiments on fully dense samples and woodpile structures with different line diameters reveal significant *topological toughness* in woodpile structures, which manifests itself in two key ways: (1) high-density woodpile structures can be twice as strong and twice as light as fully dense specimens printed with identical ink and processing parameters, and (2) low-density woodpile structures exhibit significant damage tolerance, indicated by multiple stress drops before catastrophic failure. These intriguing features are attributed to the lack of continuous crack paths across the entire sample and the physical separation of load-bearing elements in the woodpile architecture.

(iii) A simple analytical strength model captures the essence of the experiments and provide guidelines for optimal design. It is demonstrated that architected materials topology can be used as an effective tool to control the failure mechanisms in ceramic materials and select the desired combination of strength and damage tolerance.

CRediT authorship contribution statement

Lorenzo Valdevit conceived the research and secured funding. Raphael Thiraux developed and characterized the ink, developed all printing parameters, fabricated all samples, performed all the macroscale mechanical characterization, analyzed all the data, and wrote the first draft of the manuscript. Alexander D. Dupuy developed sintering parameters and performed microstructural characterization. Tianjiao Lei performed the nanoindentation experiments. Alexander D. Dupuy, Ali Mohraz, Timothy J. Rupert and Lorenzo Valdevit helped with data analysis and edited the manuscript.

Declaration of Competing Interest

The authors declare that they have no known competing financial interests or personal relationships that could have appeared to influence the work reported in this paper.

Acknowledgments

The authors would like to acknowledge financial support from the BIAM-UCI Research Centre for the Fundamental Study of Novel Structural Materials (Research Agreement #210263). Microstructural characterization was performed at the UC Irvine Materials Research Institute (IMRI), using facilities and instrumentation which are supported in part by the National Science Foundation through the UC Irvine Materials Research Science and Engineering Center (DMR-2011967).

Conflict of Interest

None.

Appendix A. Supporting information

Supplementary data associated with this article can be found in the online version at doi:10.1016/j.jeurceramsoc.2022.05.059.

References

[1] E. Feilden, D. Glymond, E. Saiz, L. Vandeperre, High temperature strength of an ultra-high temperature ceramic produced by additive manufacturing, Ceram. Int. 45 (2019) 18210–18214.
[2] B.R. Golla, A. Mukhopadhyay, B. Basu, S.K. Thimmappa, Review on ultra-high temperature boride ceramics, Progress Mater. Sci. 111 (2020).
[3] S.M. Wiederhorn, Brittle fracture and toughening mechanisms in ceramics, Annu. Rev. Mater. Sci. 14 (1984) 373–403.
[4] J. Bauer, L.R. Meza, T.A. Schaedler, R. Schwaiger, X. Zheng, L. Valdevit, Nanolattices: an emerging class of mechanical metamaterials, Adv. Mater. 29 (2017), 1701850.
[5] A. Guell Izard, J. Bauer, C. Crook, V. Turlo, L. Valdevit, Ultrahigh energy absorption multifunctional spinodal nanoarchitectures, Small 15 (2019), 1903834.
[6] L.R. Meza, S. Das, J.R. Greer, Strong, lightweight, and recoverable three-dimensional ceramic nanolattices, Science 345 (2014) 1322–1326.
[7] J. Bauer, et al., Additive manufacturing of ductile, ultra-strong polymer-derived Nanoceramics, Matter 1 (2019) 1547–1556.
[8] Gu Wendy X., J.R. Greer, Ultra-strong architected Cu meso-lattices, Extreme Mech. Lett. 2 (2015) 7–14.
[9] M. Mieszala, et al., Micromechanics of amorphous metal/polymer hybrid structures with 3D cellular architectures: size effects, buckling behavior, and energy absorption capability, Small 13 (2017), 1602514.
[10] J. Bauer, A. Schroer, R. Schwaiger, O. Kraft, The Impact of size and loading direction on the strength of architected lattice materials, Adv. Eng. Mater. 18 (2016) 1537–1543.
[11] X. Zhang, A. Vyatskikh, H. Gao, J.R. Greer, X. Li, Lightweight, flaw-tolerant, and ultra-strong nanoarchitected carbon, Proc. Natl. Acad. Sci. U.S.A. 116 (2019) 6665–6672.
[12] J. Bauer, A. Schroer, R. Schwaiger, O. Kraft, Approaching theoretical strength in glassy carbon nanolattices, Nat. Mater. 15 (2016) 438–443.
[13] J. Bauer, S. Hengsbach, I. Tesari, R. Schwaiger, O. Kraft, High-strength cellular ceramic composites with 3D microarchitecture, Proc. Natl. Acad. Sci. U.S.A. 111 (2014) 2453–2458.
[14] M.A. Skylar-Scott, S. Gunasekaran, J.A. Lewis, Laser-assisted direct ink writing of planar and 3D metal architectures, Proc. Natl. Acad. Sci. U.S.A. 113 (2016) 6137–6142.
[15] Q. Wu, M. Maire, S. Lerouge, D. Therriault, M.-C. Heuzey, 3D printing of microstructured and stretchable chitosan hydrogel for guided cell growth, Adv. Biosyst. 1 (2017), 1700058.
[16] E. Feilden, et al., 3D printing bioinspired ceramic composites, Sci. Rep. 7 (2017) 13759.
[17] B.G. Compton, J.A. Lewis, 3D-printing of lightweight cellular composites, Adv. Mater. 26 (2014) 5930–5935.
[18] G. Franchin, L. Wahl, P. Colombo, Direct ink writing of ceramic matrix composite structures, J. Am. Ceram. Soc. 100 (2017) 4397–4401.
[19] S.Z. Guo, F. Gosselin, N. Guerin, A.M. Lanouette, M.C. Heuzey, D. Therriault, Solvent-cast three-dimensional printing of multifunctional microsystems, Small 9 (2013) 4118–4122.
[20] S.-Z. Guo, M.-C. Heuzey, D. Therriault, Properties of polylactide inks for solvent-cast printing of three-dimensional freeform microstructures, Langmuir 30 (2014) 1142–1150.
[21] A.K. Grosskopf, R.L. Truby, H. Kim, A. Perazzo, J.A. Lewis, H.A. Stone, Viscoplastic matrix materials for embedded 3D printing, ACS Appl. Mater. Interfaces 10 (2018) 23353–23361.
[22] V.S. Deshpande, N.A. Fleck, M.F. Ashby, Effective properties of the octet-truss lattice material, J. Mech. Phys. Solids 49 (2001) 1747–1769.
[23] L. Rueschhoff, W. Costakis, M. Michie, J. Youngblood, R. Trice, Additive manufacturing of dense ceramic parts via direct ink writing of aqueous alumina suspensions, Int. J. Appl. Ceram. Technol. 13 (2016) 821–830.
[24] M. Acosta, V.L. Wiesner, C.J. Martinez, R.W. Trice, J.P. Youngblood, Effect of polyvinylpyrrolidone additions on the rheology of aqueous, highly loaded alumina suspensions, J. Am. Ceram. Soc. 96 (2013) 1372–1382.
[25] V.L. Wiesner, J.P. Youngblood, R.W. Trice, Room-temperature injection molding of aqueous alumina-polyvinylpyrrolidone suspensions, J. Eur. Ceram. Soc. 34 (2014) 453–463.
[26] J.E. Smay, J. Cesarano, J.A. Lewis, Colloidal inks for directed assembly of 3-D periodic structures, Langmuir 18 (2002) 5429–5437.
[27] A. M'Barki, L. Bocquet, A. Stevenson, Linking rheology and printability for dense and strong ceramics by direct ink writing, Sci. Rep. 7 (2017) 1–10.
[28] Compel, W.S. & Lewicki, J.P. Advanced methods for direct Ink write additive manufacturing, 2018.
[29] H. Yuk, X. Zhao, A New 3D printing strategy by harnessing deformation, instability, and fracture of viscoelastic inks, Adv. Mater. 30 (2018), 1704028.

[30] Feilden, E.. Additive manufacturing of ceramics and ceramic composites via robocasting, 2017.
[31] W.H. Herschel, R. Bulkley, Ronsistenzmessungen yon (ummi-BenzollGsungen), Colloid Polym. Sci. 39 (1926) 291.
[32] Md Sarker, X.B. Chen, Modeling the flow behavior and flow rate of medium viscosity alginate for scaffold fabrication with a three-dimensional Bioplotter, J. Manuf. Sci. Eng. 139 (2017).
[33] E. Feilden, E.G.-T.T. Blanca, F. Giuliani, E. Saiz, L. Vandeperre, Robocasting of structural ceramic parts with hydrogel inks, J. Eur. Ceram. Soc. 36 (2016) 2525–2533.
[34] J. Baltazar, P.M.C. Torres, J. Dias-de-Oliveira, J. Pinho-da-Cruz, S. Gouveia, S. Olhero, Influence of filament patterning in structural properties of dense alumina ceramics printed by robocasting, J. Manuf. Processes 68 (2021) 569–582.
[35] M. Asmani, C. Kermel, A. Leriche, M. Ourak, Influence of porosity on Youngs modulus and poisson's ratio in alumina ceramics, J. Eur. Ceram. Soc. 21 (2001) 1081–1086.
[36] Auerkari, P. Mechanical and physical properties of engineering alumina ceramics. *VTT Tiedotteita - Valtion Teknillinen Tutkimuskeskus* (1996).
[37] A. Krell, P. Blank, Grain size dependence of hardness in dense submicrometer alumina, J. Am. Ceram. Soc. 78 (1995) 1118–1120.
[38] D. Tabor, The Hardness of Metals, Oxford University Press,, 2000.
[39] J. Lankford, W.W. Predebon, J.M. Staehler, G. Subhash, B.J. Pletka, C.E. Anderson, The role of plasticity as a limiting factor in the compressive failure of high strength ceramics, Mech. Mater. 29 (1998) 205–218.
[40] G. Subhash, S. Maiti, P.H. Geubelle, D. Ghosh, Recent advances in dynamic indentation fracture, impact damage and fragmentation of ceramics, J. Am. Ceram. Soc. 91 (2008) 2777–2791.
[41] L.J. Gibson, M.F. Ashby, Cellular Solids, Cambridge University Press,, 1997.
[42] M. Genet, M. Houmard, S. Eslava, E. Saiz, A.P. Tomsia, A two-scale Weibull approach to the failure of porous ceramic structures made by robocasting: Possibilities and limits, J. Eur. Ceram. Soc. 33 (2013) 679–688.
[43] S.P. Timoshenko, J.M. Gere, W. Prager, Theory of elastic stability, second edition, J. Appl. Mech. 29 (1962) 220–221.